Arch Dermatol Res (2010) 302:705–715
DOI 10.1007/s00403-010-1071-2

ORIGINAL PAPER

Phenotypic profiling of keloid scars using FT-IR microspectroscopy reveals a unique spectral signature

Katherine A. Hollywood · Marlies Maatje · Iqbal T. Shadi · Alex Henderson · Duncan Angus McGrouther · Royston Goodacre · Ardeshir Bayat

Received: 20 March 2010 / Revised: 10 July 2010 / Accepted: 28 July 2010 / Published online: 11 August 2010

Abstract Keloid disease (KD) is a quasineoplastic fibroproliferative tumour of unknown origin causing a progressive, recurrent dermal lesion. KD is not homogeneous in nature and shows phenotypic structural differences between its distinct peripheral margins compared to its centre. The keloid margin is often symptomatically more active with increased dermal cellularity, compared to a symptomatically dormant and hypocellular centre of lesion. The aim of this study was to delineate the morphological components of a keloid scar tissue by measuring the differences between various anatomical locations within the keloid tissue, such as the margin and the centre of the lesion compared to its surrounding normal skin using Fourier transform infrared (FT-IR) microspectroscopy. FT-IR microspectroscopy is a technique that produces spectra with detailed molecular biochemical information inherent of the chemical structure. Chemical maps were constructed on extralesional cross sections taken from six keloid scars. H&E stained sections were used to confirm diagnosis of keloid and orientate the experimental cross sections prior to FT-IR. Spectral band assignment and principal components analysis were conducted. Distinct vibrational bands (100 spectra) were observed using FT-IR spectroscopy. Partial least squares discriminant analysis, with bootstrapping (10,000 analyses), identified whether a spectrum was from the keloid or normal tissue showing an average accuracy of 84.8%, precision of 80.4%, specificity of 76.2%, and sensitivity of 92.9%. FT-IR microspectroscopy showed significant differences in spectral profiles in keloid tissue in different anatomical locations within the cross section. We believe that this proof-of-concept study may help substantiate the use of FTIR spectroscopy in keloid diagnosis and prognosis.

Keywords Keloid disease · Abnormal raised dermal scarring · Fourier transform infrared spectroscopy · Extralesional biopsy excision · Histological diagnosis · Active periphery or margin of lesion

M. Maatje · A. Bayat (✉)
Plastic and Reconstructive Surgery Research,
Manchester Interdisciplinary Biocentre,
University of Manchester, 131 Princess Street,
Manchester M1 7DN, UK
e-mail: ardeshir.bayat@manchester.ac.uk

D. A. McGrouther · A. Bayat
Manchester Academic Health Science Centre,
Department of Plastic and Reconstructive Surgery,
University Hospital of South Manchester NHS Foundation Trust,
Wythenshawe Hospital, Southmoor Road,
Manchester M23 9LT, UK

K. A. Hollywood · I. T. Shadi · R. Goodacre
School of Chemistry and Manchester Interdisciplinary Biocentre,
The University of Manchester, 131 Princess Street,
Manchester M1 7DN, UK

A. Henderson
School of Chemical Engineering and Analytical Science,
Manchester Interdisciplinary Biocentre, University of Manchester,
131 Princess Street, Manchester M1 7DN, UK

Introduction

Keloid disease (KD) is a benign fibroproliferative tumour affecting the reticular skin, which causes a progressive, recurrent dermal tumour [20, 22]. Previous studies provide compelling evidence that genetic dysregulation plays an important role in KD development although the exact aetiopathogenesis remains unknown [6, 21]. These fibrous growths can cause significant disfigurement and unwanted symptoms, such as intense pain and pruritus [2, 20]. The

inflammation, itching, and throbbing can be especially severe during the growth phase, but even long-standing lesions may continue to have tender and painful margins compared to a more quiescent and often involuting centre [1]. Keloid disease presents a significant burden for patients and a significant therapeutic challenge for clinicians [2, 5].

Keloid disease (KD) results from an abnormal tissue response to dermal injury and is characterized by persistent growth of dermal connective tissue after re-epithelialization and extension of scar tissue beyond the original borders of the wound [24]. These scars are raised and spread beyond the margins of the original wound, invading the surrounding normal skin in a site-specific way. This is in contrast to hypertrophic scars, which are the result of an exaggerated wound healing response and stay confined to the boundaries of the original lesion [2, 20]. KD seems to be unique to humans, can occur at any age and affect individuals of all races and both sexes [2]. In addition, KD can be identified in most anatomical locations with predisposition to certain sites including the chest, shoulders, upper back, back of the neck, and earlobes [1, 2].

The histological profile of KD is characterized by the presence of thick, hyalinized, homogeneous, strongly eosinophilic bundles of collagen, haphazardly orientated in reticular dermis (Fig. 1) [24]. Keloids have a swirling nodular pattern of collagen fibres and the resulting fibrous growths invade normal dermis which can produce a fibrotic mass in the subcutaneous tissue [24].

Due to the fact that keloid scars do not regress spontaneously, plus the fact that no plausible long-term effective treatment has yet been found, research on causation, treatment options, and prognosis is of great interest [2]. A combination of surgical excision followed by intralesional steroid injection, or other adjuvant therapy, currently appears to be the most effective regimen for clinical management of KD [7]. Surgical excision alone, however, demonstrates recurrence rates between 45 and 100% [7]. We recently demonstrated that recurrence of keloid lesions can vary according to the extent of surgical excision; keloids excised intralesionally had a higher recurrence compared to those removed extralesionally [24]. In addition, there appears to be phenotypic differences between the structurally distinct peripheral margin to the centre of the keloid lesion. The margin is symptomatically more active and hypercellular as opposed to the relatively inactive hypocellular centre [24]. The aim of this study was to delineate the morphological components of an extralesionally excised keloid tissue by looking at differences in cross sections and comparing different anatomical locations within the keloid tissue using an alternative technique to histology. The main advantage would be to simultaneously image the quantity

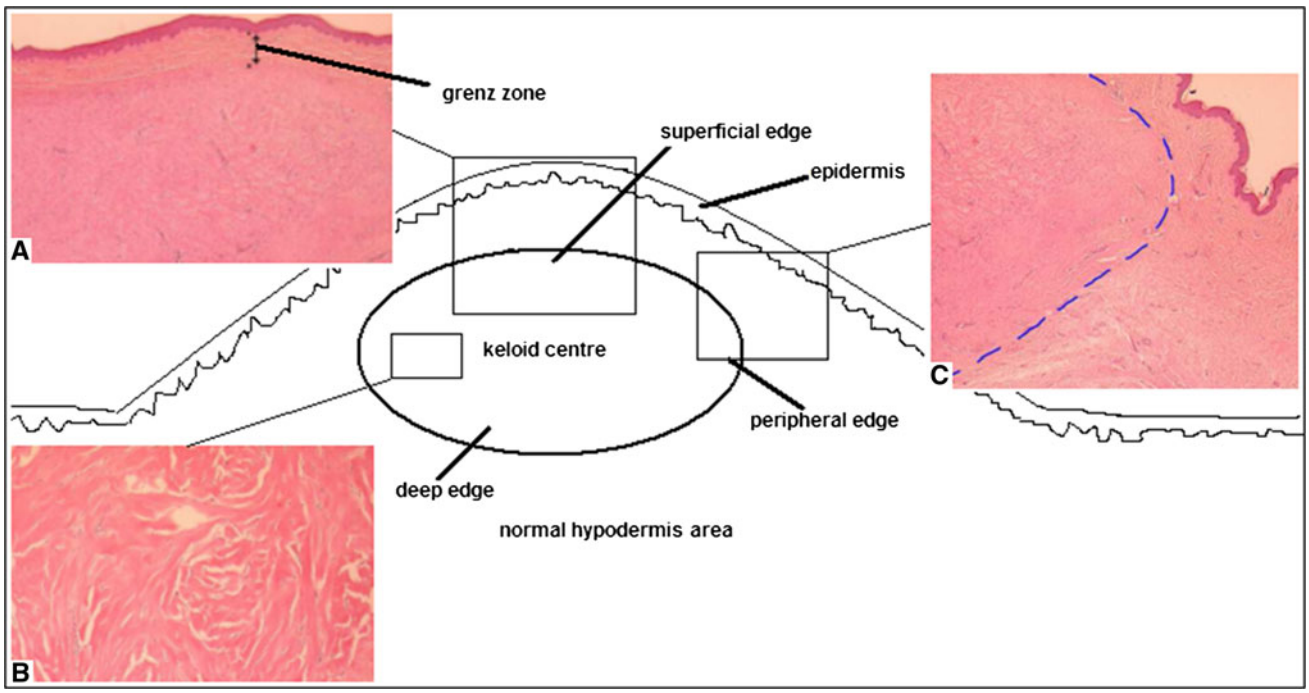

Fig. 1 Diagrammatic and histological cross section of an extralesional keloid scar including: **a** The Grenz zone in a keloid; the histological area corresponding to papillary dermis of normal dermis located between the epidermal basement membrane and the upper edge of the reticular dermis. **b** View of thick hyalinized collagen bundles typically found in middle of keloid scars. **c** Keloid with circumscribed borders (marked in *blue*) which are well-demarcated demonstrating the periphery or margin of the keloid scars

and quality of multiple components in KD in relation to normal skin using a technique with high molecular sensitivity combined with a spatial resolution down to a few micrometres.

Fourier transform infrared (FT-IR) spectroscopy is a rapid, non-destructive technique which is well suited for the analysis of human tissue samples [8, 9]. FT-IR microspectroscopy allows spectral information to be gained while maintaining the morphology of the sample by combining simple light microscopy with infrared instrumentation [10, 13, 23]. Sample preparation is minimal and therefore the possibility of losing relevant biochemical information as a function of space is minimized. In FT-IR microspectroscopy there are two general approaches: the coupling of a mercury cadmium telluride (MCT) detector allows the collection of spectra from specific areas to be acquired by combination with a light microscope; in contrast, the incorporation of a focal plane array (FPA) detector [16] permits the production of larger areas to be examined and a variety of arrays exist (e.g., 1×16, 32×32, 64×64 or 128×128 pixels) that allow the generation of infrared hypercubes to be collected in a simultaneous fashion [11]. These hyperspectral data (where each pixel contains an infrared spectrum) can be transformed into chemical maps which allow the spatial distribution of functional groups, specific chemical species [19], or disease areas using chemometrics [15] to be generated.

In this study we have applied for the first time FT-IR microspectroscopy to investigate the morphometric profiles of extralesionally excised keloid scar tissue specimens. Both MCT and FPA detectors were used and coupled to chemometric methods for the classification of keloid scars versus normal tissue using partial least squares discriminant analysis as well as chemical mapping using principal components analysis.

Materials and methods

Patients and samples

Keloid disease (KD) cases were recruited from our specialist scar service at the outpatient Department of Plastic and Reconstructive Surgery unit in South Manchester University Hospital Foundation Trust (Manchester, England, UK). All patients participating in the study were confirmed to have keloid scars both by using our stringent clinical criteria in addition to histological confirmation by a pathologist with an interest in dermatopathology. The employment of such rigorous diagnostic criteria in our recruitment protocol assured us of the correct diagnosis of all recruited individuals. This approach was taken to limit the confounding effects of disease heterogeneity and misdiagnosis potentially inherent in other scarring studies which may fail to differentiate between hypertrophic scars and KD. Therefore, the following clinical criteria were used to identify keloid disease cases as opposed to other forms of skin scarring conditions, such as hypertrophic scars. A keloid scar was defined clinically as a dermal tumour that spread beyond the margin of the original wound, continued to grow over time, did not regress spontaneously, and had been present for at least a minimum period of 1 year. In comparison, hypertrophic scars were defined as raised scars that remained within the boundaries of the original lesion, often regressed spontaneously within several months after the initial injury [24].

The local and hospital ethical committees had given approval for the study protocol and proformas. Written consent was obtained from all individuals who entered into the study. All cases were personally assessed and examined by the senior author. A full medical history was taken using a proforma and each scar lesion was examined in detail. Extralesional keloid samples were collected post surgery. Each specimen was bisected and one half of the section was snap frozen in liquid nitrogen and the other half placed in formalin fixative.

A total of six histologically proven keloid scars (see Fig. 2 for an example) were excised from four keloid patients. Specimens were collected from a variety of anatomical sites from patients of varying age, sex, and ethnicity

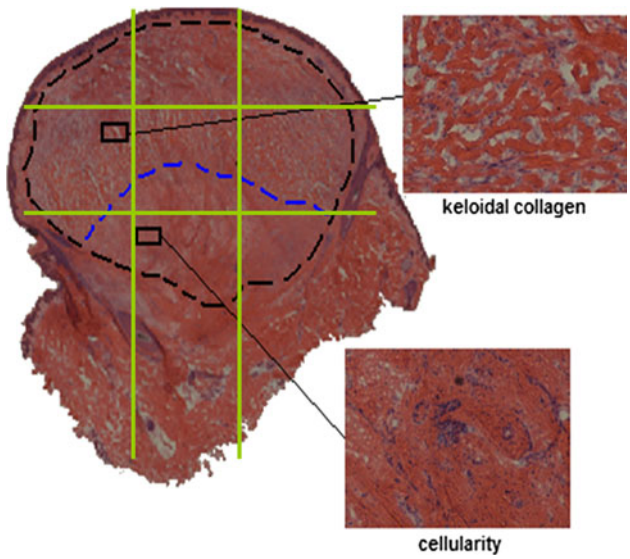

Fig. 2 This cross section of a typical keloid scar (sample number 3) excised from the chest wall demonstrates anatomical locations within the keloid scar. *Lines* in *green* show where line mapping using FT-IR spectroscopy was taken; this resulted in 38 spectra in total: 3 epidermal, 21 normal and 14 from the reticular dermis of the keloid scar. The *cyan* area shows where FT-IR chemical maps were collected from: this included 14 individual maps containing 64×64 pixels and covered an area of approximately 3.5×0.25 mm. *FT-IR* Fourier transform infrared

Table 1 Demographic details of keloid cases in the study

Sample number	Age	Sex	Race	Keloid scar anatomical location
1	20	Male	Caucasian	Shoulder
2	22	Female	Caucasian	Ear
3	45	Male	Black African	Sternum
4	45	Male	Black African	Jaw
5	36	Female	Black African	Sternum
6	36	Female	Black African	Shoulder

(Table 1). A number of additional features associated with the causation and appearance of the keloid samples were recorded using a pre-validated scar assessment proforma (Table 2) [3].

Fourier transform infrared (FT-IR) microspectroscopy

The FT-IR data were collected in transmission mode using a Bruker microscope infrared imaging system (Bruker Spectrospin Ltd., Coventry, UK), composed of an Equinox 55 module step scan Fourier transform spectrometre coupled to either (a) a mercury cadmium telluride (MCT) single point detector connected to a manually controlled *x, y*-stage, or (b) a Hyperion 3000 microscope (Bruker Optics Ltd, USA), equipped with a 64×64 liquid nitrogen cooled MCT focal plane array (MCT FPA) detector.

The MCT detector allows for the collection of *single point spectra* at chosen locations. In all MCT-driven experiments 64 coadds were collected at a resolution of 4 cm^{-1} producing absorbance spectra in the range of 4,000–600 cm^{-1}. The FPA detector can be used to collect high-resolution images of a large sample area. With a $\times 15$ IR objective lens this allows the analysis of sample areas of approx. 267 μm × 267 μm. A pixel area of 64×64 was collected equating to 4,096 spectra from each of the detector elements. Tissue mapping was conducted with a spectral resolution of 4 cm^{-1} and a spectral range of 4,000–900 cm^{-1}. A single coadd was collected and the typical acquisition time for each image was approximately 12 min.

The data were collected using routines of the OPUS 4.0 IR imaging software (Bruker Optics, USA), and then exported as ASCII files which were subsequently imported into Matlab version 7.1 (The MathWorks, Inc., MA, USA) for analysis (vide infra).

Sample preparation

Frozen tissue samples

For FT-IR analysis, specimens were snap frozen in liquid nitrogen and stored at −80°C until analysis. Frozen cross sections from the keloid scars were sectioned using a cryostat microtome (Leica CM1900, UK) at a thickness of 10 μm and air dried onto calcium fluoride (CaF_2) IR-transparent windows. Adjacent 5 μm sections were collected and air dried onto glass slides for pathological analysis by hematoxylin and eosin (H&E) staining. Digital images were obtained from the H&E stained sections using a Digital Imaging Microscope (Nikon, Eclipse 80i, Japan) at a magnification of 10×4. Individual images from each section were manually stitched together within GIMP (version 2.2.15) to allow classification of keloid and normal skin cross sections.

FT-IR data collection and chemometric analyses

MCT infrared analysis

A total of 22 line-mapping experiments were conducted from the six individual keloid slices. Line mapping was conducted both in vertical and in horizontal directions. Vertical line maps represented a transition from epidermis, through normal dermis region (termed Grenz zone), into the diseased keloid part (superficial edge → keloid centre → deep edge), and returning to normal dermis region again

Table 2 Clinical details (history and examination findings) of keloid scars

Sample number	Cause	Onset (years)	Symptoms	Colour mismatch[a]	Matt/shiny	Distortion	Texture	Contour
1	Vaccination	3	Itch and pain	Gross	Matt	Severe	Hard	Raised
2	Ear piercing	5	Itch	Slight	Matt	Moderate	Firm	Raised
3	Acne spot	1	Itch	Gross	Shiny	Severe	Hard	Raised
4	Shaving trauma	3	Itch	Gross	Shiny	Severe	Hard	Raised
5	Acne spot	2	Itch	Gross	Shiny	Severe	Hard	Raised
6	Acne spot	2	Itch	Gross	Shiny	Severe	Hard	Raised

[a] To the surrounding skin

(Figs. 1, 2). Similarly, line mapping in a horizontal direction transits from a normal region, into the diseased keloid part (peripheral edge/margin → keloid centre → peripheral edge/margin), and finally returning into a normal dermal region. In this way it was possible to categorise our measurements in the following categories, epidermis (e), normal (n), keloid (k), or doubtful provenance (d). Doubtful provenance areas were regions that could not be assigned without an element of doubt from interpretation of corresponding H&E staining or light image from the microscope. Each sample was subject to 3 or 4 line-mapping experiments, existing of a number of sampling points (mean of 12 points).

Collected spectra were collated and scaled using extended multiplicative scatter correction (EMSC) [18]. To eliminate the region of unavoidable baseline drift that occurs between ~1,650–2,000 cm^{-1} and the CO_2 absorption in the area of 2,350–2,450 cm^{-1} these sections were eliminated from analysis by removing these data regions. Principal components analysis [14] was conducted and typically three principal components (PCs) were extracted and PC loading plots were used to study variability within and between the samples and anatomical sites. All data analyses were performed within Matlab. Line-mapping data were analysed in single line maps, collated per sample, and as a large collective dataset.

Partial least squares (PLS) [17] analyses were conducted on the large collated dataset consisting of 100 spectra from the six locations on the four patients. Spectra were selected based on the collection region being clearly differentiated by microscopy as being normal tissue or keloid. PLS-discriminant analysis (PLS-DA) was performed with defined outputs as 0 = normal and 1 = keloid. In order to validate the classification, so as to avoid false discovery [4], PLS-DA bootstrapping was performed in PLS-DA using the replacement method [25]; thus 'on average' 37% of samples were used for testing and 63% of samples were used for training. Bootstrapping was performed 10,000 times on the data. On the 10,000 test data only (i.e., the validation data, not the training set) statistics can be performed and this results in a confusion matrix, box and whisker plot, and a receiver operator characteristic curve.

FPA image analysis

The previously obtained H&E stains (Fig. 2) were used to identify sample KS34 as the best example of a keloid section, and therefore this section was selected for chemical image analysis. A vertical line image was collected by collating 14 individual FPA images (i.e., 14 by 64 × 64 pixels). The areas were selected using the visible light images provided by the microscope on the Hyperion 3000 microscope and were manual aligned using the *x*–*y* stage. The line map incorporates a transition from normal epidermis to dermal keloid areas and returning to normal skin morphology.

Upon collection the individual spectral datacubes were concatenated to produce a single large dataset within Matlab. As some of the pixels were deemed bad (i.e., they gave a signal irrespective of whether infrared absorbance was occurring) these specific intensities were removed by filtering the entire dataset and setting any intensity value with absorbance >4.9999 to zero (these are later removed prior to PCA; see below). This process removes large domineering spikes in the data while not blanking the pixel entirely. The spectra were then summed to produce a total intensity image.

To normalise the data for PCA any pixel greater than zero was set to 100% and anything less than zero was set to −100%. This established that 0 is truly zero and its colour will match any other zero in the dataset. Wavenumber regions contributing a high level of varying noise corresponding to water and CO_2 interferences were eliminated by removing ranges 4,000–3,700 cm^{-1} and 2,450–2,250 cm^{-1}, respectively. Bad pixels were removed completely prior to PCA which was performed using MATLAB's princomp.m routine. Bad pixels were reinserted into the missing positions in the PC scores matrix with all intensity values set to zero. The datacube was reshaped and PC scores false colour coded to generate chemical maps, and corresponding PC loadings plotted for the first 9 PC scores.

Finally, nine wave number bands were selected as displaying significant variation between normal and keloid tissue regions (see below). The area under the peak of the given wavenumber bands were integrated, following linear baseline removal, and the subsequent images plotted.

Results

Histological findings

The epidermis, the Grenz zone (the intermediate papillary zone between the epidermis and the reticular dermis), the deep reticular dermis of keloid samples ($n = 6$) region as well as the equivalent regions in normal skin were identified and confirmed by a histopathologist (Fig. 1a, b, c). The thickness of the Grenz zone varied between the different histological sections (Fig. 1a). However, the epidermis remains unaltered at the top in all lesions (Fig. 1a, c) and the middle of each Keloid scar demonstrated a swirling nodular pattern of fibres and thick hyalinized collagen bundles (Fig. 1b). Figure 2 demonstrates a cross section of a keloid lesion which shows the typical, abnormal thick collagen fibres ("keloid collagen") at the centre of lesion, the lower part, however, is characterized by a diffuse cellularity.

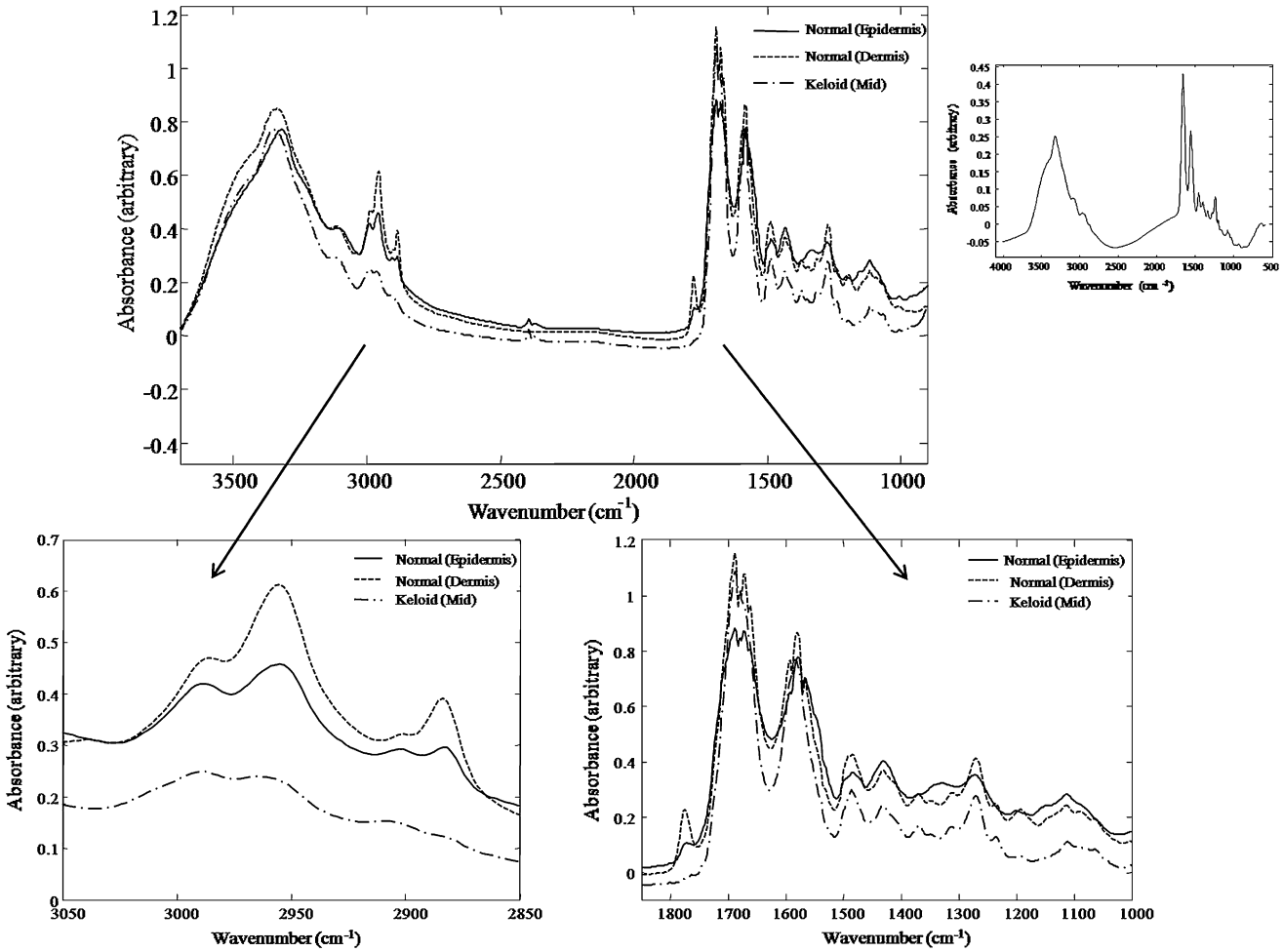

Fig. 3 Typical FT-IR absorbance spectra collected from normal skin tissue, and keloid epidermal and dermal regions. Offset graph demonstrates a spectrum of Collagen. *FT-IR* Fourier transform infrared

The margin or periphery of the cross sections appeared more cellular.

FT-IR microspectroscopy

Vibrational bands from cellular proteins, membrane lipids, and nucleic acids were observed, providing molecular information relating to the structure and concentration of these materials within a cell. Typical representative FT-IR spectra are shown in Fig. 3. These spectra were obtained from normal regions in the hypodermis or from keloid regions in the cross section, and the arrows indicate the significant differences between the keloid and the normal skin spectrum. Also included is a spectrum of collagen, which is known to be predominant in skin and in keloids.

Chemometric analyses

PCA was carried out on all line-mapping experiments to obtain PCA scores plot. A typical PC scores plot is shown in Fig. 4a. In this example, as in all others (data not shown), these scores plot generally show discrimination between normal and keloid tissue; where present, spectra from the epidermis and dermis were clearly differentiated from normal and keloid tissue (data not shown). The spectral variance in the keloid was less marked than the normal regions (Fig. 4).

PC loading plots were also generated and these allow the spectral features that are used in the production of the PCA to be revealed. The example shown in Fig. 4b is typical, where spectral features from lipids were larger in the normal tissue (positive in PC1) than in the keloid tissue (negative in PC1) which seemed to resemble the spectrum of pure collagen (Fig. 3d).

Based on these findings, using an unsupervised learning method we trained PLS-DA to discriminate between keloid and normal tissue as detailed above. The results from the 10,000 bootstrap analyses for the test data only are shown in Fig. 5, where it can be seen that the average ROC is 0.922 which is important for differentiation. Moreover, the

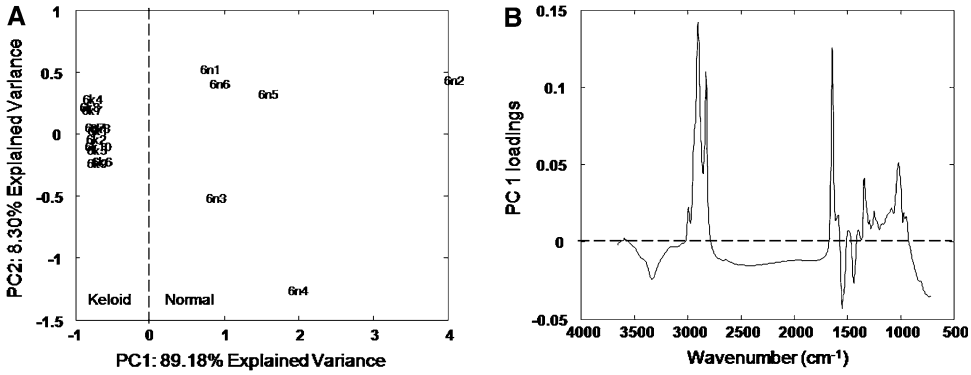

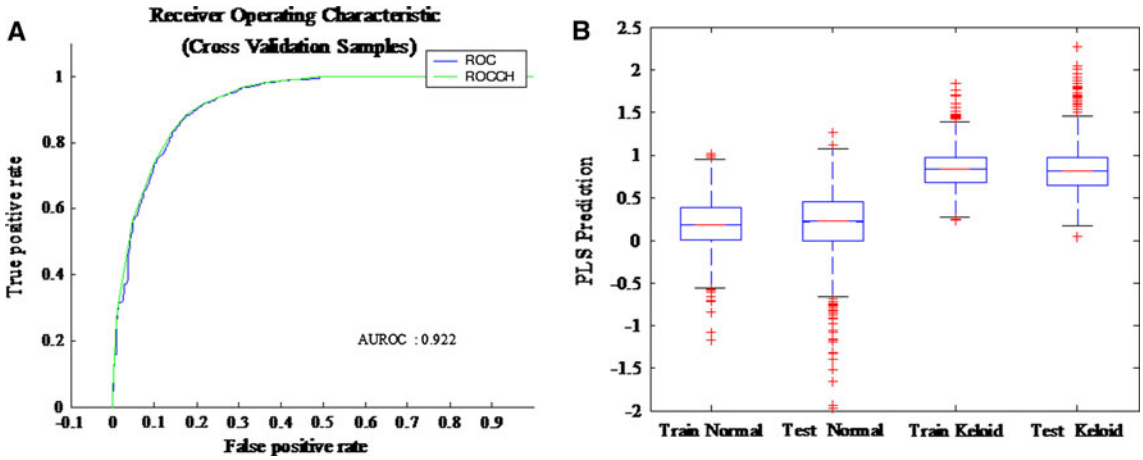

Fig. 4 **a** PCA scores plot from one of sample number 4 with lines (2nd *horizontal line*) showing clear differentiation between normal tissue and keloid scar. **b** Corresponding PC1 loading plots showing features that are discriminatory. *PCA* principal components analysis, *PC*1 principal component 1

Fig. 5 Results from PLS-DA bootstrap analysis from 100 spectra selected from six samples. **a** Average receiver operating characteristic plots from the test data only from the 10,000 models and **b** Box whisker plots showing the data from all training and test data from the 10,000 PLS-DA models that were constructed. *Boxes* represent the lower median and upper quartiles. *Whiskers* represent the range or 1.5× the length of the box, whichever is shorter. Outliers (+) are the values out of the whisker range. *PLS-DA* partial least squares-discriminant analysis

box whisker plot shows the results for all 10,000 models and also shows that PLS-DA can readily differentiate between normal tissue and keloid scars.

FT-IR microspectroscopic imaging

The results of the spectral area maps correspond well with the tissue histological sections (Fig. 6). These maps provide detailed biochemical information, not readily available from other techniques (Table 3); these images indicate regions of lipid, amide, and phosphate content within different areas in the tissue section (Fig. 6), and PCA on the total chemical map allowed other features to be revealed by inspecting the corresponding PC loading matrices (Fig. 7).

Discussion

This study for the first time demonstrates that FT-IR microspectroscopy shows significant differences in spectral profiles from keloid tissue in different anatomical locations within the cross sections. Distinct vibrational bands (100 spectra from six samples) were observed for each lesion using FT-IR spectroscopy. Partial least squares discriminant analysis, with appropriate validation using bootstrapping (10,000 bootstrap analyses), identified whether a spectrum was from the keloid or normal tissue showing an average accuracy of 84.8%, precision of 80.4%, specificity of 76.2%, and sensitivity of 92.9%.

FT-IR spectroscopy is a novel and robust approach for keloid disease diagnostics [9, 10] and this has been complemented and in this study our findings were verified by routine histopathology. The classification and ‘orientation’ of the KD tissue slices were confirmed with the aid of complementary H&E-stained slides as a direct reference for each KD sample studied. In addition these KD H&E slides played an important role during the interpretation of the results, in particular, during the chemical-mapping process.

As is common in FT-IR studies the spectra are qualitatively very similar (Fig. 3) and generally show only subtle quantitative spectral differences between different tissue types or between disease and normal cells. Coupled with

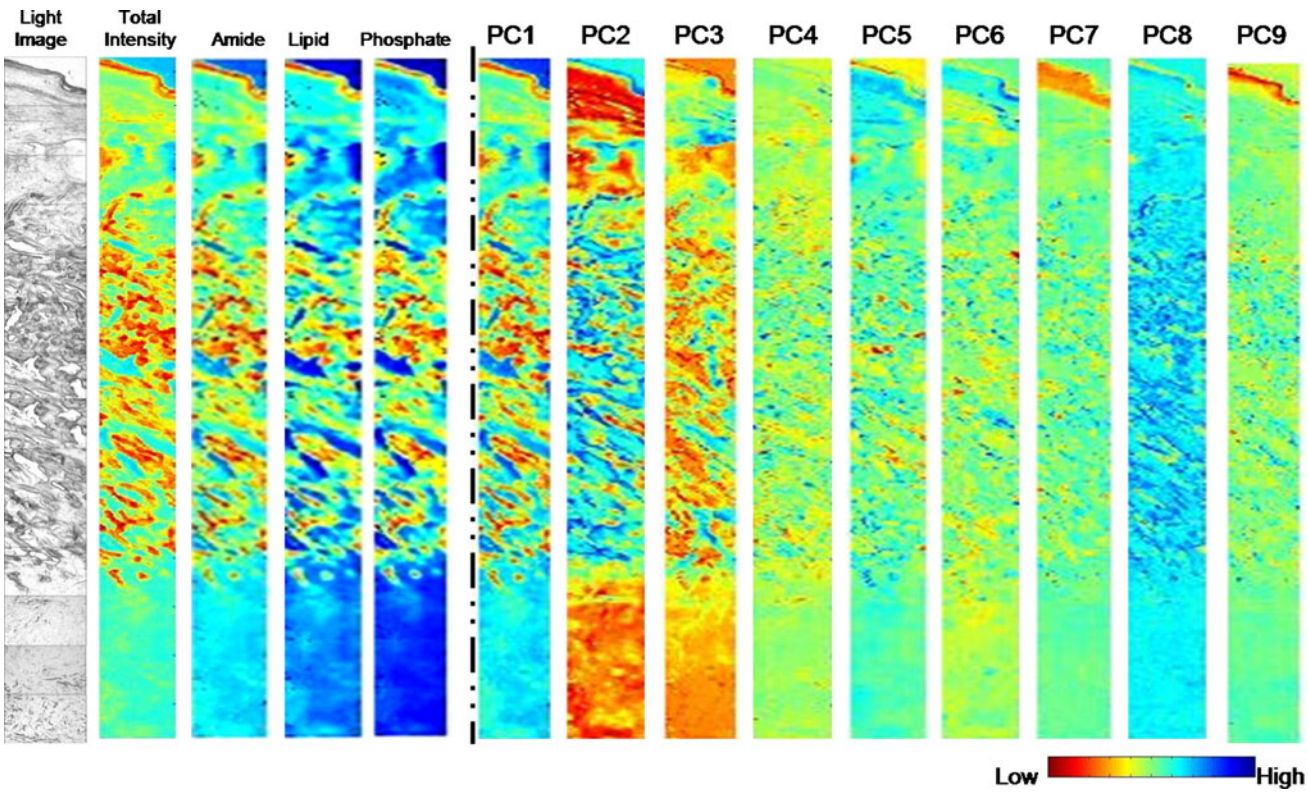

Fig. 6 Chemical image plots from sample number 3 of chest wall generated from IR microspectroscopy. The light image is shown from the unstained tissue and corresponds to the area detailed in Fig. 2. The first four false colour coded maps are from the sum of the total IR signal, area under lipid, amide, and phosphate bands, respectively. The next nine image maps represent the first 9 PC scores. *IR* infrared, *PC* principal component

Table 3 Tentative infrared vibrational band assignments for regions of interest

Region	Wave number range (cm^{-1})	Mid point (cm^{-1})	Assignment
1	3,030:2,995	3,012	Amide B (N–H stretching) from protein
2	2,990:2,880	2,935	Asymmetric CH_2 stretching from lipid
3	2,875:2,830	2,852	Symmetric CH_2 stretching from lipid
4	1,780:1,720	1,750	C=O stretch from lipid
5	1,715:1,600	1,657	Amide I (80% C=O stretch)
6	1,590:1,490	1,540	Amide II (60% N–H in plane bend, 40% C–N stretch)
7	1,480:1,430	1,455	CH_2 scissoring from lipid
8	1,260:1,215	1,237	Amide III (40% C–N stretch, 30% N–H in plane bend, 20% methyl-C stretch)
9	1,195:1,135	1,165	Asymmetric PO_2^- stretch from nucleic acids

the inherent large data size (these FT-IR spectra were typically represented by 1,764 data points) there is a reliance on chemometric approaches for analysis of these multivariate data.

The first stage in the chemometric analysis was to analyse each sample individually using an unsupervised method. In such an approach, the algorithm is 'unaware' of the data and the main aim is to assess the natural variance in the data presented. PCA is a reliable approach for this and the projection method generates new axes called principal components (PCs) which are not correlated. PCs summarise the variance in the data and find any natural structure; which was the difference between KD and normal skin. Figure 4 shows an example for sample 4, where the PC scores plot (Fig. 4a) shows clear differentiation between normal tissue and KD in the first PC; that is to say the axes which explain the most natural variance (89.2% total explained variance).

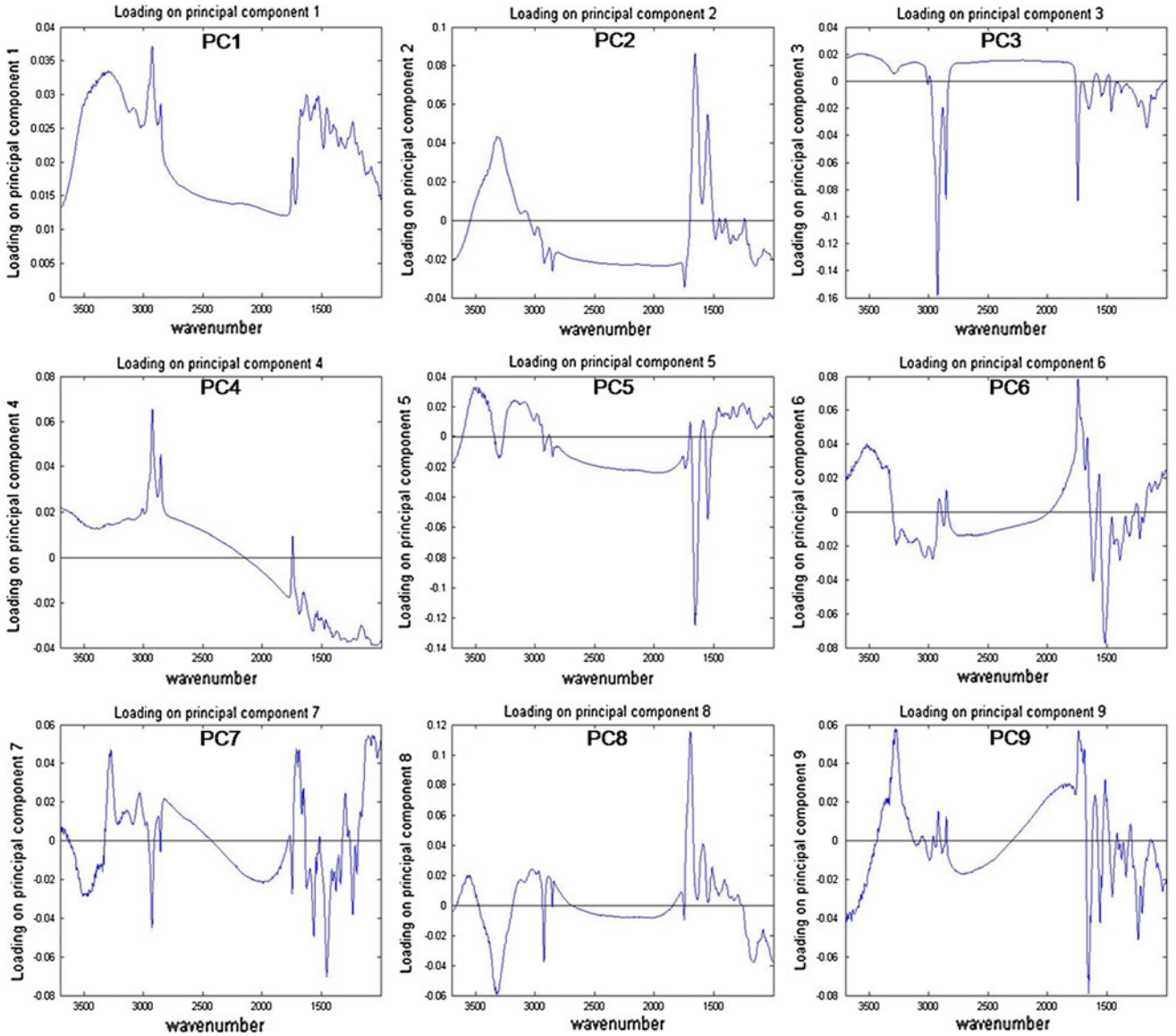

Fig. 7 Corresponding PC loading plots from the PCA of IR microspectroscopy in Fig. 6. *PC* principal component, *PCA* principal components analysis, *IR* infrared)

During PCA there is a simultaneous projection in the variable space and these PC loading plots can reveal (bio) chemical information about which features are important for separations in PC score plots. The result loadings plot for the KS34 analysis is shown in Fig. 4b; positive areas are increased in normal tissue (as the samples are located in the positive part of PC scores 1) and vice versa, negative loadings are increased in the keloid scar. The negative part of the PC1 loadings plot shows peaks at ~1,600 and ~1,450 cm^{-1} which can be attributed to amide I (C=O) and II (N–H), in addition to a broad peak at ca. 3,250 cm^{-1} which is another N–H stretch from proteins. These correlate well with the FT-IR spectrum of pure collagen type I (Fig. 3d) which is perhaps not surprising given that collagen is not only found in skin but is also densely laid down in KD tissue. In contrast, the positive loadings are predominantly from lipids. The three vibrational bands from 3,050 to 2,750 cm^{-1} are from C–H_x and the very sharp band at 1,780 cm^{-1} is from C=O (a constrained carbonyl vibration) from where the acyl chain joins the polar head group.

Similar results were found from the analyses of the other five samples (data not shown). In order to distinguish tissue spectra from normal skin or KD irrespective of patient or tissue location, we used the supervised learning method of PLS-DA. In this process the algorithm is given information on the pathological state of the spectrum's location and we encoded normal tissue as a '0' and keloid tissue as '1'. As some of the spectra were of doubtful origin, that is to say

the pathological status of the border was difficult to interpret, these were removed from the model, this resulted in 100 spectra in which we had high confidence in their provenance. As only 100 spectra were taken from 6 samples it is possible to over fit the data analysis [4] and therefore in order to validate the PLS-DA classification model, bootstrapping was performed using the replacement method [25]. Bootstrapping was performed 10,000 times on the data. Figure 5 shows the average ROC curve which has an area of 0.922. In addition, box whisker plots for the training and test data for the normal and keloid tissues are shown from the 10,000 models. This again shows excellent distribution of results and the average statistics on these models were an accuracy of 84.8%, precision of 80.4%, specificity of 76.2%, and sensitivity of 92.9%. Finally, the true positive rate was 92.9%, true negative rate 76.2%, false positive was 23.8%, and false negative 7.1%.

The H&E section in Fig. 2 highlighted sample 3, KS34 from the sternum, as the best example of a keloid section, therefore this section was selected for chemical image analysis using FT-IR microspectroscopy. An area of approximately 3.5 × 0.25 mm was analysed by IR and this was achieved by collecting 14 separate 64 × 64 pixel datacubes using the FPA detector on the microscope and aligning the cubes one on top of another (Fig. 2). In chemical mapping, a derivative value for each spectrum is first generated and the intensity response at each wavenumber was summed; thus the whole IR spectrum at each pixel is collapsed into a single value. These are then used to generate false colour maps and in this instance we encoded a high value as red and a low value as blue. In order for the images to look less pixelated we used interpolated shading in the mapping function in Matlab. This is known as Gouraud shading [12] and is piecewise linear where the colour in each pixel varies linearly and interpolates with the corner values from the surrounding 8 pixels. The results are displayed as a series of chemical maps and Fig. 6 shows these for the total IR signal collected (4,000–600 cm^{-1}), the CH_x from the lipid (3,000–2,750 cm^{-1}), the amide I and II bands (1,700–1,500 cm^{-1}), and the phosphate content (1,350–1,250 cm^{-1}) representing predominantly nucleic acids. The total IR signal shows that the keloid scar is very dense in material as is the epidermis, whilst the normal tissue at both interfaces with the keloid is not as rich in spectral features. The lipid, protein, and nucleic acid chemical maps show very similar spectral features with the obvious exception of the changes in intensity of these bands. The fact that these images are largely congruent means that alternate methods are needed to reveal any subtle spectral features.

Thus, we applied PCA on these images, 57,344 spectra were analysed (equating to 14 × 64 × 64 spectra × 3,400 wavenumbers i.e., 194,969,600 data points), and extracted the first 9 PCs and their corresponding loading matrices (Fig. 7). It is clear from these PC chemical maps that PCs 1, 2, 3, 7, and 9 relate clearly to histological features (Fig. 2). PC1 highlights the keloid epidermis and dermis as these pixels have high values in PC1, however, this resembles the total IR signal and as no scaling was used prior to PCA this is not surprising. In contrast PC2 highlights the keloid dermal region well as the PC2 score is low for the keloid reticular region and positive for normal tissue including the epidermis; the corresponding loadings plot is shown in Fig. 7 (a protein spectrum correlates with collagen). The PC3 loadings plot corresponds to lipids and the features are similar to those found previously in the analysis of a different tissue (Fig. 4; sample 4: KS34), the scores plot of this feature is uniformly high in the normal tissue but rather granular within the keloid. PCs 7 and 9 largely highlight the keloid epidermis only and many spectral features are evident in the corresponding loadings plots. From the PCA it is clear that many spectral features are changing within the keloid, and not just collagen alone. In combination with the visible inspection above (lipid, protein, and nucleic acid) nine spectral areas of interest are potentially important in this pathological process and these are highlighted in Table 3. In conclusion, in this study we have demonstrated the proof-of-concept that FT-IR microspectroscopy displays significant differences in spectral profiles in keloid tissue in different anatomical locations. These findings may help substantiate the use of FTIR spectroscopy in keloid diagnosis with potential implication for disease prognosis.

Acknowledgments We would like to acknowledge the support of the following organizations for this study: NIHR (UK). In addition we would like to specially thank the GAT Family Foundation, and Steve and Kathy Fitzpatrick for generous funding and support. K.A.H. thanks Stiefel Laboratories (U.K.) Ltd. for her studentship and R.G. is very thankful to UK BBSRC for funding.

Conflict of interest The authors state no conflict of interests.

References

1. Bayat A, Arscott G, Ollier WER, Ferguson MWJ, Mc Grouther DA (2004) Description of site-specific morphology of keloid phenotypes in an Afrocaribbean population. Br J Plast Surg 57:122–133
2. Bayat A, McGrouther DA, Ferguson MWJ (2003) Skin scarring. Br Med J 326:88–92
3. Beausang E, Floyd H, Dunn KW, Orton CI, Ferguson MWJ (1998) A new quantitative scale for clinical scar assessment. Plast Reconstr Surg 102:1954–1961
4. Broadhurst D, Kell DB (2006) Statistical strategies for avoiding false discoveries in metabolomics and related experiments. Metabolomics 2:171–196
5. Brown BC, McKenna SP, Siddhi K, McGrouther DA, Bayat A (2008) The hidden cost of skin scars: quality of life after skin scarring. J Plast Reconstr Aesthet Surg 61:1049–1058
6. Brown JJ, Bayat A (2009) Genetic susceptibility to raised dermal scarring. Br J Dermatol 161:8–18

7. Durani P, Bayat A (2008) Levels of evidence for the treatment of keloid disease. J Plast Reconstr Aesthet Surg 61:4–17
8. Ellis DI, Dunn WB, Griffin JL, Allwood JW, Goodacre R (2007) Metabolic fingerprinting as a diagnostic tool. Pharmacogenomics 8:1243–1266
9. Ellis DI, Goodacre R (2006) Metabolic fingerprinting in disease diagnosis: biomedical applications of infrared and Raman spectroscopy. Analyst 131:875–885
10. Fabian H, Thi NAN, Eiden M, Lasch P, Schmitt J, Naumann D (2006) Diagnosing benign and malignant lesions in breast tissue sections by using IR-microspectroscopy. Biochim Biophys Acta Biomembr 1758:874–882
11. Fernandez DC, Bhargava R, Hewitt SM, Levin IW (2005) Infrared spectroscopic imaging for histopathologic recognition. Nat Biotechnol 23:469–474
12. Gouraund H (1971) Continuous shading of curved surfaces. IEEE Trans Comput C-20:623–629
13. Hollywood K, Brison DR, Goodacre R (2006) Metabolomics: current technologies and future trends. Proteomics 6:4716–4723
14. Jolliffe IT (1986) Principal component analysis. Springer, New York
15. Lasch P, Haensch W, Naumann D, Diem M (2004) Imaging of colorectal adenocarcinoma using FT-IR microspectroscopy and cluster analysis. Biochim Biophys Acta Mol Basis Dis 1688:176–186
16. Lewis EN, Treado PJ, Reeder RC, Story GM, Dowrey AE, Marcott C, Levin IW (1995) Fourier transform spectroscopic imaging using an infrared focal-plane array detector. Anal Chem 67:3377–3381
17. Martens H, Naes T (1989) Multivariate calibration, 1st edn. Wiley, Chichester
18. Martens H, Nielsen JP, Engenlsen SB (2003) Light scattering and light absorbance separated by extended multiplicative signal correction. Application to near-infrared transmission analysis of powder mixtures. Anal Chem 75:394–404
19. Patel SA, Currie F, Thakker N, Goodacre R (2008) Spatial metabolic fingerprinting using FT-IR spectroscopy: investigating abiotic stresses on *Micrasterias hardyi*. Analyst 133:1707–1713
20. Seifert O, Mrowietz U (2009) Keloid scarring: bench and bedside. Arch Dermatol Res 301:259–272
21. Shih B, Bayat A (2010) Genetics of keloid scarring. Arch Dermatol Res 302:319–339
22. Shih B, Garside E, McGrouther DA, Bayat A (2010) Molecular dissection of abnormal wound healing processes resulting in keloid disease. Wound Repair Regen 18:139–153
23. Sulé-Suso J, Skingsley D, Sockalingum GD, Kohler A, Kegelaer G, Manfait M, El Haj AJ (2005) FT-IR microspectroscopy as a tool to assess lung cancer cells response to chemotherapy. Vib Spectrosc 38:179–184
24. Tan KT, Shah N, Pritchard SA, McGrouther DA, Bayat A (2010) The influence of surgical excision margins on keloid prognosis. Ann Plast Surg 64:55–58
25. Westerhuis JA, Hoefsloot HCJ, Smit S, Vis DJ, Smilde AK, van Velzen EJJ, van Duijnhoven JPM, van Dorsten FA (2008) Assessment of PLSDA cross validation. Metabolomics 4:81–89